Journal of Applied Polymer Science

Synthesis and Spectroscopic and Photoconduction Characteristics of Coaxial Poly[2-methoxy-5-(2′-ethylhexyloxy)−1,4-phenylene vinylene] Single-Walled Carbon Nanotube Films with Ohmic-like Transport Attributes

Tahereh Hosseini, Nikolai A. Kouklin
Department of Electrical Engineering and Computer Science, University of Wisconsin-Milwaukee, Milwaukee Wisconsin 53201
Correspondence to: N. A. Kouklin (E-mail: nkouklin@uwm.edu)

ABSTRACT: Highly luminescent, core–shell, single-walled carbon nanotube–poly[2-methoxy-5-(2′-ethylhexyloxy)−1,4-phenylene vinylene] (MEH-PPV) one-dimensional networks were synthesized by a multicycle unstable micellization method. The current–voltage data indicated that the charge transport within the nanowire network remained Ohmic, with the differential conductance scaling linearly with temperature in the temperature range of about 120 to 300 K. Further analysis based on the comparative study involving photoluminescence and Raman spectroscopic tests pointed to interchain interactions and nanotube–polymer interface as primary factors influencing the electronic characteristics of the processed samples. Likewise, steady-state photoconduction tests confirmed that the heterointerface played a dominant role behind the increased photoresponse induced by exciton annihilation at a low bias regime. The study helped us identify the underlying physical mechanisms that controlled the optical, electrical, and photoconduction properties of the MEH-PPV–carbon nanotube heteronetworks. Potentially, this will open a door to the development of next generation, low-cost, all-organic nanooptoelectronic devices and systems. © 2013 Wiley Periodicals, Inc. J. Appl. Polym. Sci. **2014**, *131*, 40029.

KEYWORDS: composites; properties and characterization; synthesis and processing

Received 15 June 2013; accepted 29 September 2013
DOI: 10.1002/app.40029

INTRODUCTION

For their highly favorable device characteristics, processability, and cost-relief advantages, organic electronic materials remain a mainstream venue of nanomaterials research. Improvements in such areas as charge mobility, spin-valve operation, and light emission can potentially lead the way and enable the use of conjugated polymers either alone or in combination with other crystalline nanomaterials such as carbon nanotubes (CNTs) in future nanoelectronics, spintronics, and nanooptoelectronics.[1–3] Single-walled carbon nanotubes (SWNTs), in particular, share one-dimensional atomic arrangements and advanced electronic characteristics that are commensurate with those of conjugated polymers. To this end, recent spectroscopic dynamics studies have confirmed ultrafast (∼400 fs) charge transfer in poly(3-hexylthiophene) SWNT heterojunctions.[4,5] The fast charge separation at the polymer–nanotube interface combined with the ease of polymer processing can potentially open a door to the realization of lightweight, high-efficiency solar cells and photodetectors.[6] Because of its excellent stability and strong visible-range luminescence, poly[2-methoxy-5-(2′-ethylhexyloxy)−1,4-phenylene vinylene] (MEH-PPV) is primarily considered for a host of light-emitting device applications. Although similarly to other conjugated polymers, the chemical structure and conjugation length primarily determine the optical and electrical properties of MEH-PPV, as extensively documented in the literature. The performance of polymer-based solid-state devices is also strongly influenced by environmental effects, MEH-PPV packing, and chain morphology. Current processing routes, such as the direct dispersion of nanotubes in the polymer matrix, spin-coating, inkjet printing, and surface spraying,[7–9] not only lack control on the resulting polymer–nanotube arrangement but also remain unsuitable for the engineering core–shell heterojunctions required to achieve efficient charge injection/separation. To address this limitation, additional approaches to synthesizing coaxial-type polymer–nanotube heterostructures have been offered; the list includes electrospinning, linker-based, and direct-surface-coating techniques.[10–12] However, the schemes typically require treatment conditions that are not exactly commensurate with the processing routes of MEH-PPV, and as a result, poor light-emission efficiencies are demonstrated. In this study, an unstable micellization strategy was used to produce highly luminescent, core–shell, one-dimensional SWNT–MEH-PPV nanoheterostructures.[13,14] The

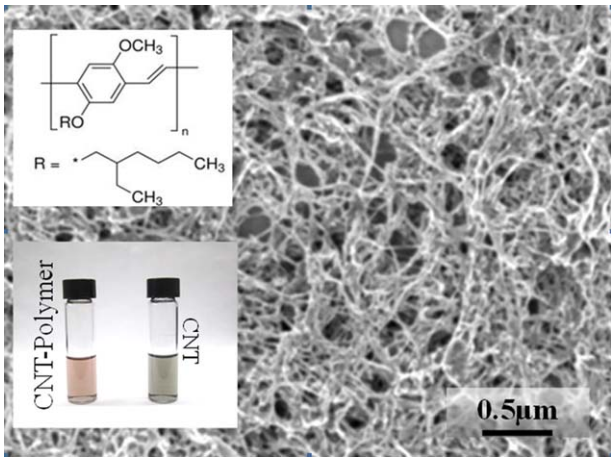

Figure 1. Top-view SEM image of the MEH-PPV encased CNT films. The lower inset shows a digital photo of the suspensions of the SWNTs and MEH-PPV–SWNTs. [Color figure can be viewed in the online issue, which is available at wileyonlinelibrary.com.]

optical, electrical, and light-emission characteristics of the resulting nanostructured composites and the role of the SWNT–MEH-PPV heterojunction behind the photoresponse were studied by means of transport, photoluminescence (PL), photoluminescence–excitation (PLE), Raman spectroscopic, and steady-state photoconduction tests, the results of which are presented and discussed later. Among other findings, a detailed analysis of Raman spectrum of the composite sample pointed to a partial stabilization of the SWNT defects by SWNT–polymer π-staking interactions.

EXPERIMENTAL

HiPCo SWNTs featuring diameters and band gaps (semiconducting components) of about 0.7–1.3 nm and 0.8–1.3 eV, respectively, were acquired from Carbon Nanotechnologies. MEH-PPV was obtained in the powder form from Sigma-Aldrich and had an average molecular weight of 200,000 and a polydispersity close to unity. The optoelectronic properties of this polymer are known to be strongly dependent on the conformational disorder, which primarily affects the exciton localization and interchain energy transfer rate and can give rise to blinking effect, characteristic of semiconductor quantum dots. In collapsed conformations, the dipole–dipole based interchain energy transfer prevails over intrachain transfer because of a significant reduction in the average distances between the chains. The use of a proper solvent, such as chloroform in case of MEH-PPV, is mandatory for the production of extended chain conformations, which can help suppress exciton migration within the polymer matrix and away from active device regions. This is to negatively affect photocarrier generation and collection yields.

To ensure optimal structural arrangement, MEH-PPV was dissolved in a chloroform ($\sim$0.1 mg/mL) under continuous agitation with a vortex shaker for 3–5 min. To produce MEH-PPV-encased CNT micelles, the MEH-PPV chloroform solution was next mixed with a nanotube aqueous suspension in about a 1:5 proportion, whereas the mixture was subject to sonication for about 3–5 min. The first step helped to create individually suspended, small-diameter nanotube bundles that later acted as reaction centers for the noncovalent immobilization of the MEH-PPV molecules driven by hydrophobic–hydrophobic interactions. To increase the yield, we removed the unreacted polymer micelles by discarding the supernatant at the end of each centrifugation cycle.

The MEH-PPV-encased nanotube samples were next collected and dropcast onto a clean, highly polished c-Si substrate. According to Figure 1, which presents a top-view field emission scanning electron microscope (Hitachi S4800, $\sim$1 kV) image, the resulting films exhibited no apparent long- or short-range order typical of unprocessed SWNT random-network films. However, the SEM images of the processed samples appeared on average about 30% brighter; this was indicative of increased charge relaxation times associated with the limited conductivity of MEH-PPV. Successful formation of the shell was also confirmed in the course of fast, high-resolution SEM imaging/inspections of the samples.

RESULTS AND DISCUSSION

To study the structural characteristics and impacts of polymer immobilization on the electronic characteristics of the processed nanotube networks, the resulting samples were subject to comparative Raman spectroscopic studies performed with a Renishaw micro-Raman spectrometer operating in conjunction with a 20× optical microscope. The spectra were excited with a 633-nm line of a He–Ne laser. The backscattered light was collected and dispersed by a spectrometer onto a a thermoelectrically cooled charge-coupled device detector array. In the high-frequency part, the Stocke's Raman spectrum of the SWNTs assembled on top of Au substrates was clearly dominated by graphite mode (G; $\sim$1592 cm^{-1}) and defect mode (D; $\sim$1310 cm^{-1}).

Compared to the unprocessed nanotube spectrum, the spectra of the MEH-PPV films produced with the dropcast method consisted of several Raman-active bands: the out-of-plane CH-bending mode of the vinylene group (966 cm^{-1}), the C—C stretching and C—H in-plane bending modes (1110 cm^{-1}), the C=C stretching band of the phenyl ring (1283 cm^{-1}), the C=C stretching coupled to a C—H bending of the vinyl group (1310 cm^{-1}), and the C—C symmetric stretching vibration of the phenyl ring (1585 cm^{-1}).[15,16]

To enhance the signal-to-noise ratio, the MEH-PPV nanotube micelles were extracted dielectrophoretically (DEP) and self-assembled into continuous networks with two planar Au electrodes separated by a gap of about 100 μm. During the DEP self-assembly process, the intensity of the Raman-active bands coming from the micelles was continuously monitored. The Raman signal was found to evolve nonmonotonically in time, and its time dependence could be best approximated by a Heaviside step function [$\theta(t - t_0)$, where t_0 stands for a characteristic micelle assembly time, typically $\sim$3–5 min]. Figure 2(left top) presents the Raman spectra of the MEH-PPV–nanotube micelles past about 3 min of assembly. An order of magnitude improvement in the signal-to-noise ratio observed past t_0 was in part

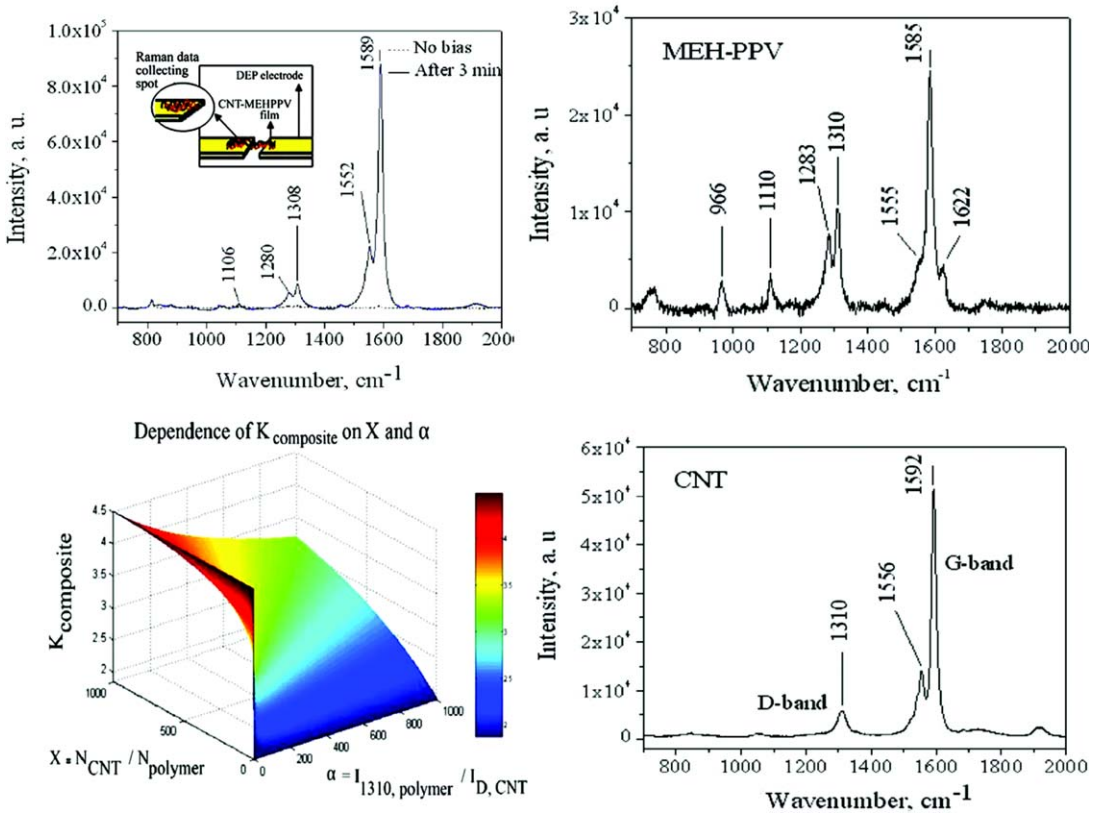

Figure 2. (Left top) Raman spectra of the MEH-PPV encapsulated films obtained without the application of bias (black) and 3 min after the application of alternating-current bias (blue; ~0.5 V and ~200KHz); (right top and bottom) Raman spectra of the MEH-PPV and SWNTs, respectively; and (left bottom) two-dimensional plot of k_{comp} versus X and α; these confirmed that $k_p \leq k_{comp} \leq k_{CNT}$ ($k_p = 1.84$ and $k_{CNT} = 4.5$). [Color figure can be viewed in the online issue, which is available at wileyonlinelibrary.com.]

attributed to the substrate-enhanced Raman scattering effect (SERS). The Raman bands shown in Figure 2(left and right top) with peaks at about 963, 1107, 1283, and 1307 cm^{-1} were MEH-PPV-associated bands, whose positions were found to be redshifted by about 3 cm^{-1} relative to their bulk positions. Furthermore, the band at about 1589 cm^{-1} of the composite samples exhibited a spectral profile that closely mimicked that of the G band of the SWNTs. The double-peak band at about 1280–1308 cm^{-1}, also shown in Figure 2(left top), was a distinctive characteristic of MEH-PPV, with both results thus serving as a confirmation that the structures consisted of core–shell SWNT–MEH-PPV bundles.

To better understand the Raman spectra of the composite samples and the role the constituent components played, we quantified a content-related contribution by taking into consideration the separate contribution of the most prominent Raman bands of the MEH-PPV and SWNTs. For this, an integral intensity ratio coefficient (k_{comp}) is introduced as follows:

$$k_{comp} = \frac{N_{CNT} I_G^{CNT} + N_{polym} I_{1585}^{polym}}{N_{CNT} I_D^{CNT} + N_{polym} I_{1310}^{polym}} \quad (1)$$

where N_{CNT} and $N_{polymer}$ are the net average numbers of the SWNTs and polymer molecules contributing to the Raman intensity and I_G^{CNT}, I_D^{CNT}, I_{1310}^{polym}, and I_{1585}^{polym} are the Raman scattering efficiencies/cross sections of the G and D bands of the nanotubes, C═C stretching coupled to C—H bending mode of the vinyl group, and C—C symmetric stretching vibration of the phenyl ring of the polymer, respectively.

With $X = N_{CNT}/N_{polymer}$, $k_{CNT} = \frac{I_G^{CNT}}{I_D^{CNT}}$, and $k_p = \frac{I_{1585}^{polym}}{I_{1310}^{polym}}$, eq. (1) is simplified to become

$$k_{comp} = \frac{X k_{CNT} I_D^{CNT} + k_p I_{1585}^{polym}}{I_D^{CNT} + I_{1310}^{polym}} \quad (2)$$

where $0 \leq X < +\infty$, where X is the nanotube-to-polymer content ratio. With $\alpha = \frac{I_{1585}^{polym}}{I_D^{CNT}}$, the final formula for $k_{composite}$ can be written as a parameterized function of X:

$$k_{comp}(\alpha, x) = \frac{k_{CNT} X + k_p \alpha}{X + \alpha} \quad (3)$$

It is instructive to consider several key limiting cases. First, when the nanotube content-based contribution dramatically exceeds that of the polymer, one obtains $N_{CNT} I_D^{CNT} \gg N_{polymer} I_{1585}^{polym}$ and, therefore, $X \gg \alpha$. Because in general, $k_p \approx k_{CNT}$, eq. (3) yields $k_{comp} = k_{CNT}$, as expected. On the other hand, when $X \ll \alpha$, eq. (3) yields $k_{comp} = k_p$. Furthermore, k_{comp} remains a monotonic function of X and does not have

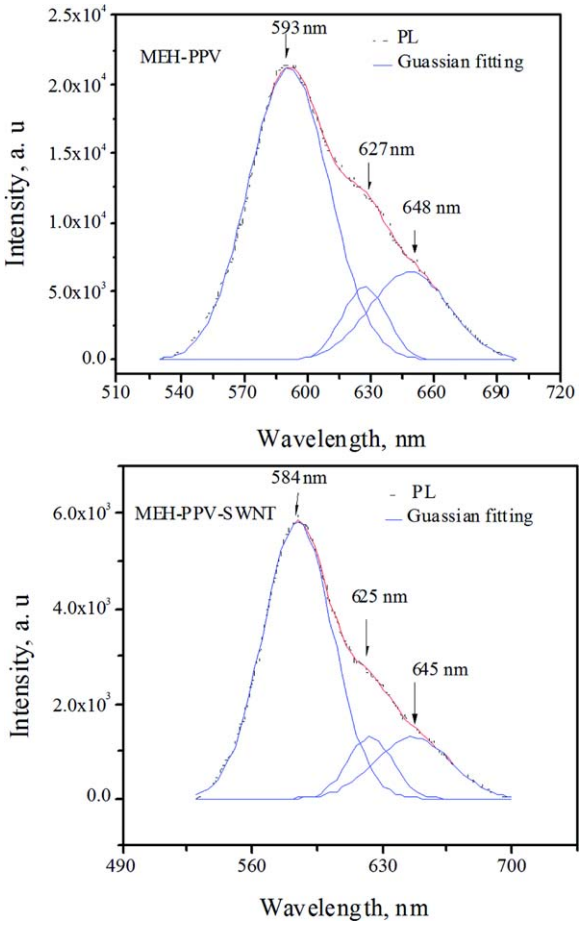

Figure 3. The PL spectra of the MEH-PPV film (top) and MEH-PPV–SWNT (bottom) are shown in black. The results of the Gaussian spectral fits are shown in blue and red. [Color figure can be viewed in the online issue, which is available at wileyonlinelibrary.com.]

any extrema points on the whole X interval, independent of α. With separately obtained experimental Raman data, $k_p = 1.8$ and $k_{CNT} = 4.5$ ($k_p < k_{CNT}$), the range of k_{comp} is set as follows: $k_p \leq k_{comp} \leq k_{CNT}$. Figure 2 (left bottom) presents a MATLAB plot of $k_{composite}$ obtained based on eq. (1). Although $k_{composite}$ is generally expected to depend on the optical characteristics of the sample, there is no *a priori* reason to believe that the Raman scattering cross sections of the SWNTs and MEH-PPV themselves were affected differently, which in turn suggests that the range of $k_{composite}$ should have remained unaffected.

However, with $k_p = 1.8$ and $k_{CNT} = 4.5$ (experimental data), one obtains $k_{comp} = 6.8 > k_{CNT}$, with the result coming into contradiction with the predictions of the linear superposition model discussed previously. The Raman tests done separately on the DEP-collected SWNT samples failed to confirm any significant increase in the G/D intensity ratio; thus, we needed entirely exclude both DEP and SERS effects as the possible origin of $k_{comp} > k_{CNT}$. Combined, this suggests that the mechanism behind the unexpected increase of k_{comp} was most likely related to a partial stabilization of the SWNT defects via SWNT–polymer π-staking interactions.

To probe the light-emission characteristics of the composite samples, PL spectroscopic tests were next performed comparatively on MEH-PPV and MEH-PPV-encased SWNTs. The resulting PL spectra were decomposed into individual bands with the least squares Gaussian fitting routine. Three PL bands (Figure 3)) were identified as a zero-phonon line and its two vibronic progressions.[17] Although the full width at half-maximum was found to be very similar for all of the samples, the zero-phonon PL band underwent a blueshift of about 30 meV in the composite samples; this was attributed to an internal structural arrangement of the polymer. With the results of the thickness-dependent PL tests,[18] the average polymer intermolecular distance was estimated to be about 20 nm in the MEH-PPV nanotubes versus about 10 nm in the polymer-only samples. The increase in the average interchain distance prevented excitons from migrating to lower energy emitting segments; this was the likely reason behind the blueshift of the zero-phonon PL peak position observed experimentally.

In addition to PL measurements, we carried out PLE measurements by monitoring emission at a wavelength of 585 nm while continuously changing the excitation wavelength from 360 to 550 nm. Unlike that of PL, the PLE spectrum of the composite sample (Figure 4), the bottom had a profile that was drastically different from that of the MEH-PPV film (Figure 4, top). Among some of the distinctive features that are worth mentioning is the broadening of the PLE band of the composite sample, which was attributed to a newly emerged, weak PLE band with a peak position at about 517 nm, as clearly revealed by the Gaussian decomposition. This PLE band was absent in the polymer-only films and did not result by itself in any new PL band, and therefore, its origin was tentatively prescribed to the electronic states formed in the proximity of the MEH-PPV SWNT interface. Apart from this, an increase in the strength of the PLE band at about 469 nm was clearly noticed in the spectrum of the SWNT–polymer films (Figure 4, bottom). Because the free carrier density remained low in MEH-PPV, the electric field produced at the interface of the two materials remained only weakly screened and inevitably led to a Stark redshift of the excitonic transitions involving $1A_g$ and $1B_u$ states. However, no redshift was observed in the PL data, as it was possibly counterbalanced by a blueshift stemming from a decrease in the average intermolecular distance in the composite films, as discussed previously. Finally, it should be also mentioned that MEH-PPV had C_{2h} symmetry, and therefore, one-photon optical transitions remained and allowed only for the states of the opposite parity. The electric field generated by the interface dipoles, however, could induce the coupling of the $1A_g$ state to an even parity and a higher lying energy state; this allowed excitonic transitions $1A_g \rightarrow mA_g$. However, according to the results presented in Figure 4, no new, higher lying PLE bands were observed; this indicated that the same parity transitions were likely to stay forbidden in the processed samples.

To assess the charge-transport characteristics, the film was placed across about a 50-μm gap formed between two Ag pads, which were thermally evaporated on top of a SiO_2 layer about 300 nm thick that formed on top of the cSi substrate. For temperature-dependent transport measurements, the devices

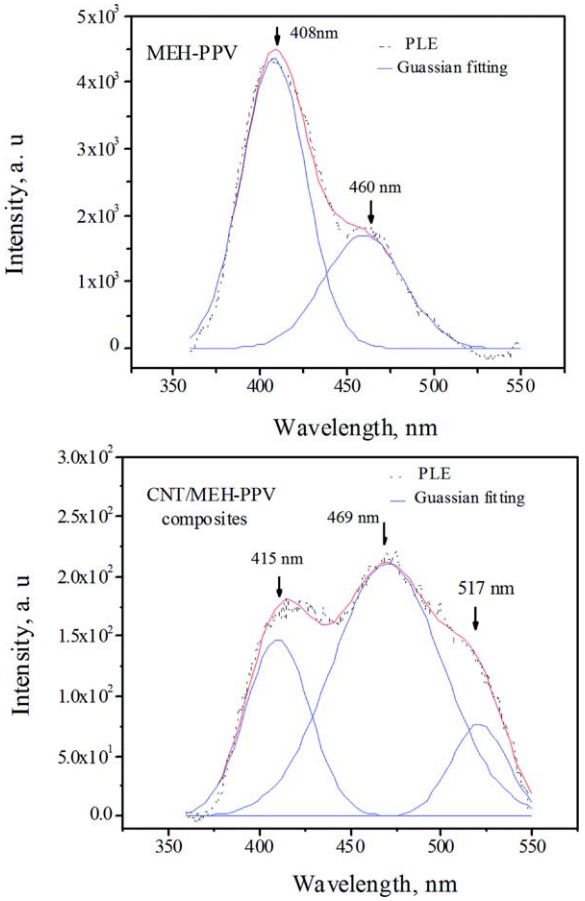

Figure 4. PLE spectra of the MEH-PPV film (top) and the MEH-PPV–nanotube network (bottom). The results of Gaussian spectral fits are shown in blue and red. [Color figure can be viewed in the online issue, which is available at wileyonlinelibrary.com.]

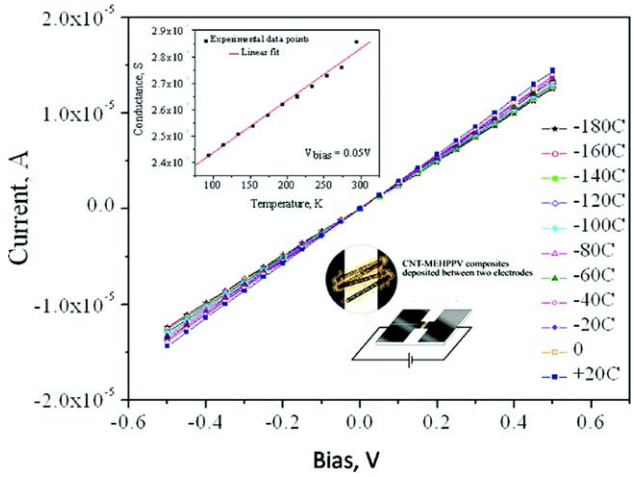

Figure 5. *I–V* characteristics of the MEH-PPV–nanotube network obtained in a temperature range of −180°C to 20°C. The left inset shows the G versus *T* plot obtained at a bias of about 0.05 V. [Color figure can be viewed in the online issue, which is available at wileyonlinelibrary.com.]

were mounted in a heating/cooling stage (Instec HCS302), and the current–voltage (*I–V*) characteristics were acquired with a Keithley 236 source–measure unit. The *I–V* characteristics collected by variation of the temperature (*T*) from −180 to 20°C during the sweeping of an applied bias from −0.5 to 0.5 V (-Figure 5) were nonrectifying and indicated that the transport within the core–shell SWNT network was not induced by variable-range-hopping, thermally assisted tunneling across polymer or nanotube–nanotube junctions.[19] Also, the device operated as a simple resistive element, with its resistance approaching about 30 KΩ in the dark (Figure 5, with the inset plots showing the differential conductance of the MEH-PPV nanotube network and G as a function of *T*).

Although in our case, G was found to change linearly with *T;* in the case of similar nanotube networks, the dependence of G on *T* was sublinear, that is, given by $G \approx T^{\alpha}$, where α was about 0.57.[20] It was clear that although the charge transport within composite samples was still controlled by a highly conductive nanotube bundle backbone, it was no longer governed by a Luttinger liquid mechanism, as in the case of pure nanotube bundle networks.[20] The obtained $G \approx T$ trend also required us to rule out polaron hopping as a possible charge-transport mechanism. The Ohmic-type conductivity was attributed to the presence of electronic states at the nanotube–polymer interface, which facilitated charge injection and transport between adjacent nanotube bundle segments.

We probed the photoconduction response and characteristics by carrying out *I–V* measurements. The samples were uniformly illuminated with a white light source (emission range/wavelengths of 420–650 nm, optical power density ≈ 5 mW/cm^2). The obtained photo *I–V* characteristics are shown in Figure 6 and remained similar to the dark *I–V* characteristics

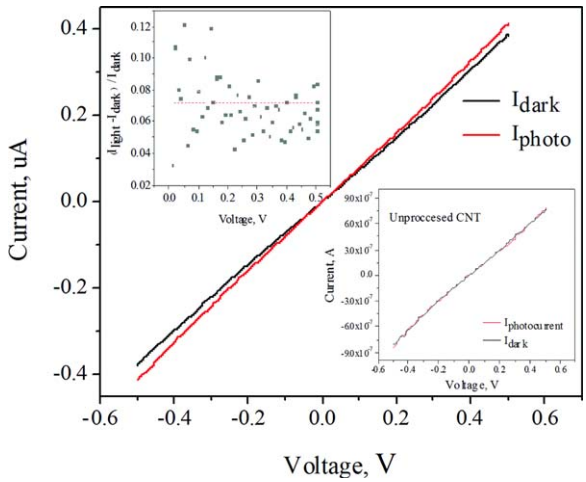

Figure 6. *I–V* characteristics of the MEH-PPV–SWNT film in the dark (red) and under white-light illumination (black). The left inset shows $(I_{light} - I_{dark})/I_{dark}$ versus the applied bias I_{light} and I_{dark} stand for currents under illumination and at dark, respectively. The increase in the photocurrent was about 7% (red line). The right inset shows the *I–V* characteristics of the unprocessed nanotubes sample obtained similarly. [Color figure can be viewed in the online issue, which is available at wileyonlinelibrary.com.]

of the SWNTs; this confirmed that the photoconduction of the composite samples was primarily controlled by the nanotube bundle backbone. The photoresponse measured as a ratio of I_{light}–I_{dark} to I_{dark} where I_{light} and I_{dark} stand for currents under illumination and at dark, (Figure 6, inset) averaged out to about 7%; this significantly exceeded the noise floor of the instrument and the photoresponse of the nanotube networks themselves. Because the photoresponse did not exhibit any dependence on the source-to-drain bias and the photocurrent could already be registered at a bias of only about 50 mV, the photocurrent was likely to be a result of exciton annihilation by a dipole electric field that existed at the nanotube–polymer interface. The resulting excess free carriers were then swept away by the external field and collected by the electrodes.

CONCLUSIONS

In summary, highly luminescent MEH-PPV core–shell nanotube planar networks with Ohmic-like transport attributes were successfully engineered with a high yield with an unstable micellization strategy. According to *I–V* tests, the transport remained Ohmic with the variation of differential conductance as a linear function of the temperature in the temperature range of about 120–300 K. Further analysis involving the PL and PLE tests revealed that the degree of interchain interactions and the presence of a nanotube–polymer interface strongly influenced the light-emission characteristics and underlying excitation–emission processes in the processed samples. Finally, the direct-current photoconduction tests indicated that the nanotube–MEH-PPV interface played a prominent role in the photocarrier generation and relatively strong photoconduction response of the composite samples. Thus, this study opens a door to the design of all-organic low-cost nanooptoelectronic devices and systems based on MEH-PPV nanotube networks and bundles.

REFERENCES

1. Galliaras, M.; Friend, R. *Phys. Today* **2005**, *58*, 53.
2. Forero, S.; Nguyen, P. H.; Brutting, W.; Schwoerer, M. *Phys. Chem.* **1999**, *1*, 1769.
3. Dougherty, S.; Liang, *J. Nanotechnology* **2009**, *20*, 295301.
4. Stranks, S. D.; Weisspfennig, C.; Parkinson, P.; Johnston, M. B.; Herz, L. M.; Nicholas, R. J. *Nano Lett* **2011**, *11*, 66.
5. Ham, M. H.; Paulus, G. L.; Lee, C. Y.; Song, C.; Kalantar-zadeh, K.; Choi, W.; Han, J. H.; Strano, M. S.. *ACS Nano* **2010**, *4*, 6251.
6. Romero, D. B.; Carrard, M.; de, Heer W. H.; Zuppiroli, L. *Adv. Mater.* **1996**, *8*, 899.
7. Chang, T.; Musikhin, S.; Bakueva, L.; Levina, L.; Hines, M.; Cyr, P.; Sargent, E. *Appl. Phys. Lett.* **2004**, *84*, 4295.
8. Yu, Z.; Barbara, P. *J. Phys. Chem. B* **2004**, *108*, 11321.
9. He, G.; Li, Y.; Yang, Y. *Appl. Phys. Lett.* **2002**, *80*, 4247.
10. Zhao, L.; Li, Y.; Liu, Z.; Shimizu, H. *Chem. Mater.* **2010**, *22*, 5949.
11. Liu, J.; Wang1, T.; Uchida2, T.; Kumar, S. *J. Appl. Polym. Sci.* **2005**, *96*, 1992.
12. Shi, D.; Lian, J.; He, P.; Wang, L.; vanOoij, W.; Schulz, M.; Liu, Y.; Mast, D. *Appl. Phys. Lett.* **2002**, *81*, 5216.
13. Chowdhary, D.; Kim, W.; Kouklin, N. *Small* **2007**, *3*, 226.
14. Kang, Y.; Taton, A. *J. Am. Chem. Soc.* **2003**, *125*, 5650.
15. Sakamoto, A.; Furukawa, Y.; Tasumi, M. *J. Phys. Chem.* **1992**, *96*, 1490.
16. Piacenza, M. *Chem. Phys. Chem.* **2009**, *10*, 1284.
17. Kong, F.; Wu, X.; Huang, G.; Yang, Y.; Yuan, R.; Yang, C.; Chu, Paul; Siu, G. *J. Appl. Phys.* **2005**, *98*, 074304.
18. Mirzov, O.; Scheblykin, I. *Phys. Chem. Chem. Phys.* **2006**, *8*, 5569.
19. Kim, G. T.; Choi, E. S.; Kim, D. C.; Suh, D. S.; Park, Y. W.; Liu, K.; Duesberg, G.; Roth, S. *Phys. Rev. B* **1998**, *58*, 16064.
20. Momari, M.; Hosseini, T.; Kouklin, N. *Nano* **2012**, *7*, 1250026.